Submitted to Cancer Science (Original Research Article)

BRCA1 haploinsufficiency impairs iron metabolism to promote chrysotile-induced mesothelioma via ferroptosis-resistance

Yaguang Luo[1], Shinya Akatsuka[1], Yashiro Motooka[1], Yingyi Kong[1], Hao Zheng[1], Tomoji Mashimo[2, 3], Tatsuhiko Imaoka[4] and Shinya Toyokuni[1, 5, *]

[1] Department of Pathology and Biological Response, Nagoya University Graduate School of Medicine, 65 Tsurumai-cho, Showa-ku, Nagoya 466-8550, Japan; [2] Division of Animal Genetics, Laboratory Animal Research Center, Institute of Medical Science, The University of Tokyo, Tokyo 108-8639, Japan; [3] Division of Genome Engineering, Center for Experimental Medicine and Systems Biology, Institute of Medical Science, The University of Tokyo, Tokyo 108-8639, Japan; [4] Department of Radiation Effects Research, National Institute of Radiological Sciences, National Institutes for Quantum Science and Technology, 4-9-1, Anagawa, Inage-ku, Chiba 263-8555, Japan; [5] Center for Low-temperature Plasma Sciences, Nagoya University, Furo-cho, Chikusa-ku, Nagoya 464-8603, Japan

Manuscript: 29 pages (5,386 words); 8 figures; 1 table; 6 supplementary tables; 5 supplementary figures.

Short running title: BRCA1 and mesothelioma

Conflict of interest: ST is the associate editor of Cancer Science. The remaining authors have no conflict of interest.

All correspondence to Shinya Toyokuni M.D., Ph.D. at the Pathology and Biological Responses. Nagoya University Graduate School of Medicine, 65 Tsurumai-Cho, Showa-Ku, Nagoya, 466-8550, Japan; Tel: +81-52-744-2086; Fax; +81-52-744-2091; E-mail; toyokuni@med.nagoya-u.ac.jp

Abstract

Malignant mesothelioma (MM) is still a social burden associated with asbestos exposure. Local iron accumulation thereby represents the major pathogenesis, followed by oxidative DNA strand breaks and genomic alterations in the mesothelium. BRCA1 is a critical component of homologous recombination repair directed to DNA double-strand breaks. Whereas *BRCA1* germline mutation is an established risk for breast/ovarian cancer, its role in MM development remains to be elucidated. Murine *Brca1* mutant models thus far have not reproduced human phenotypes. However, a rat *Brca1* mutant model (Mut; *L63X*/+) recently reproduced them at least partially. Here we describe the differential induction of MM in *Brca1* mutant rats by intraperitoneal injection of chrysotile or crocidolite. Only Mut males injected with chrysotile revealed a promotional effect on mesothelial carcinogenesis in comparison to *wild-type* and/or females, with all the MMs *Brca1*-haploinsufficient. Array-based comparative genomic hybridization of MMs disclosed a greater extent of chromosomal deletions in *Brca1* mutants, including *Cdkn2a/2b* accompanied by *Tfr2* amplification, in comparison to *wild-type* tumors. Mutant MMs indicated iron metabolism dysregulation, such as increase in catalytic Fe(II) and Ki67-index as well as decrease in Fe(III) and ferritin expression. Simultaneously, mutant MMs revealed ferroptosis-resistance by upregulation of Slc7A11 and Gpx4. At an early carcinogenic stage of 4 weeks, induced Brca1 expression in mesothelial cells was significantly suppressed in chrysotile/Mut in comparison to crocidolite/Mut whereas significant preference to iron with decrease in Fe(III) has been already established. In conclusion, chrysotile exposure can be a higher risk for MM in *BRCA1* mutant males, considering the rat results.

(250 words)

Keywords: BRCA1, asbestos, malignant mesothelioma, iron metabolism, ferroptosis

Abbreviation

aCGH	array-based comparative genomic hybridization
BM	biphasic mesothelioma
BSA	bovine serum albumin
DMT1	divalent metal transporter 1
EM	epithelioid mesothelioma
FBS	fetal bovine serum
FFPE	formalin-fixed paraffin-embedded
FISH	fluorescent *in situ* hybridization
FTH/FTL	ferritin heavy chain/ferritin light chain
GPX4	glutathione peroxidase 4
HBOC	hereditary breast-ovarian cancer syndrome
H&E	hematoxylin and eosin
HPF	high power field
HR	homologous recombination
IHC	immunohistochemistry
ip	intrapetitoneal(ly)
IRP/IRE	iron-regulatory protein(s)/iron-responsive element
MM	malignant mesothelioma
Mut	mutant (rat *Brca1 L63X*/+ in most contexts)
8-OHdG	8-hydroxy-2′-deoxyguanosine
RIPA	radioimmunoprecipitation assay
ROS	reactive oxygen species
SD	*Sprague-Dawley*
SDS-PAGE	sodium dodecyl sulfate-polyacrylamide gel electrophoresis
SM	sarcomatoid mesothelioma
Tfr1/Tfr2	transferrin receptor 1/transferrin receptor 2

UICC	Union for International Cancer Control
WT	*wild-type*
xCT	cystine/glutamate antiporter (Slc7A11)

1. Introduction

Cancer is a leading cause of human mortality worldwide (https://www.who.int/news-room/fact-sheets/detail/cancer). Among various cancers with poor prognosis, malignant mesothelioma (MM) originating from mesothelial cells covering somatic cavities reveals an epidemiologically distinct link with asbestos exposure [1]. Though all the asbestos was banned in developed countries, chrysotile (white asbestos) is still used in developing countries due to economical merits [2, 3]. Incidence of MM is expected to increase with an extended lifespan worldwide [4]. Recent studies clarified that local iron deposition causing oxidative damage, including DNA double-strand breaks (DSBs) [5, 6], is a major pathogenesis leading eventually to ferroptosis-resistance [7, 8]. *BRCA1*, a responsible tumor suppressor gene for the hereditary breast-ovarian cancer (HBOC) syndrome [9], provides a pivotal component for the homologous recombination repair of DSBs [10]. However, the association of *BRCA1* to MM carcinogenesis is still unelucidated [11] whereas studies on familial MM syndrome have identified *BAP1* (BRCA1-associated protein-1) [12] as responsible [13]. Here we for the first time undertook to evaluate the significance of *BRCA1* in MM carcinogenesis.

After the discovery of BRCA1, a variety of murine models were genetically engineered unfortunately with failure [14]. Recently, *Brca1*(*L63X*/+) rat model was established, which showed significant susceptibility to radiation-induced breast cancer [15], as well as to ferric nitrilotriacetate-induced renal cancer [16-18]. This iron-dependent carcinogenic process of MM can be mitigated by redox-inactive iron chelators [19] or phlebotomy [20]. In this study, we used this *Brca1* (*L63X*/+) rat model with *ip* injection of asbestos to assess the impact of *Brca1* germline mutation on the development of MM.

Simultaneously, we performed subacute *in vivo* experiments and cell experiments to explore the possible underlying mechanisms to determine fiber-associated differences in mesothelial carcinogenesis. We found that Brca1

haploinsufficiency promotes MM development in rats only in the case of chrysotile exposure in males.

2. Materials and methods

2.1 Animals

Brca1$^{L63X/+}$ (Mutant; Mut) rats were generated by inbreeding *wild-type Sprague-Dawley* rats (CLEA Japan; Tokyo, Japan) and *Brca1* Mut rats [15]. Rats with homozygous *Brca1*$^{L63X/L63X}$ alleles were embryonic lethal [14, 17]. Thus, we used heterozygous *Brca1*$^{L63X/+}$ and *wild-type* rats in the present experiments.

2.2 Rat carcinogenesis experiment

114 male and female *Brca1* Mut and *wild-type* Jcl/SD rats were used (*Brca1* Mut male N = 29, female N = 28; *Brca1 wild-type* male N = 28, female N = 29). The total amount of 10 mg crocidolite or chrysotile A (Union for International Cancer Control, UICC) was suspended in 5% BSA (015-27053, Wako)/0.9% NaCl solutions and subjected to *ip* administration to the rats at 5, 6, and 7 weeks (3, 3 and 4 mg, respectively) **(Figure S1A)**. *Brca1* Mut rat model has been described previously [17]. Primers to determine *Brca1* genotypes are as follows: *Brca1*-F (5'-TGCAGGTAAGTGTAATTTTCATAGG-3'), *Brca1*-Ftag (5'-GGACCTTCCCAGTGTCCTTA-3'), *Brca1*-R (5'-CCGATGTGCATGGTACTGTC-3'). The representative result of the genotype shows either one band of 572 bp (*Brca1*$^{+/+}$) or two bands of 572 and 252 bp (*Brca1*$^{L63X/+}$) **(Figure S1B)**. The same amount of 5% BSA/0.9% NaCl solution without asbestos fibers were injected into the control group. After the injection, the rats were maintained in plastic cages with 12-h day/night cycle and with free access to food (CE-2, CLEA Japan) and water under specific pathogen-free condition. Body weights were recorded regularly until a maximum of 110 weeks. When rats died, they were immediately subjected to

a complete autopsy. In addition, if the rats exhibited significant weakness, > 20% of body weight loss within one month, or have significant bloody ascites with diagnostic paracentesis, they were euthanized and underwent a complete dissection. During the dissection, macroscopic inspection and tissue collection were performed. Tumors and major organs were fixed in 10% phosphate-buffered formalin and embedded in paraffin. Further, fresh tumor and organ samples were immediately frozen in liquid N_2 and preserved at -80 ^{o}C, which were used for immunoblot, array-CGH, sequencing and quantitative PCR analyses. The animal experiment committee of Nagoya University Graduate School of Medicine approved these animal experiments.

2.3 Subacute carcinogenesis experiments

The design of the subacute experiments was the same as *section 2.2*, except that the observation was 4 weeks. In addition to formalin fixation, the mesothelium layer on the surface of the liver was collected by the method described [21], and used in the subsequent experiments.

2.4 Macroscopic and histopathological analysis

During the dissection, we took macroscopic photos to evaluate the dispersion of the tumor. MMs presenting only epithelioid or sarcomatoid subtype were recorded as epithelioid (EM) or sarcomatoid (SM), respectively. MMs with both epithelioid and sarcomatoid subtypes (≥ 10%) were recorded as biphasic (BM). Nuclear grade as a malignancy index was determined as the sum of nuclear atypia and mitotic count scores as described [20] **(Figure S2C)**. Several variants of epithelioid or sarcomatoid subtypes were classified as described [20, 22] **(Figure S2AB)**. In this experiment, each MM variant with an area of ≥ 10% was counted, and the weighted average of all variants in proportion to their nuclear grades was the nuclear grade of each MM **(Table S3)**.

2.5 Acquisition of mesothelial and mesothelioma cells

Primary mesothelial cells were obtained from freshly resected mesentery as described [23] after modification. MM cells were collected in two ways, either by cultivating severed and washed MMs directly in fresh 37 °C DMEM (043-30085, Wako) containing 10% FBS (S1810-500, Biowest) and 1% Antibiotic-Antimycotic Mix (09366-44, Nacalai) or from bloody ascites. Regardless of the method, the isolated MM cells were cloned into cell lines, which were fixed with 4% paraformaldehyde (PFA) (43368, Thermo Scientific) and confirmed by the expression of mesothelial markers before use.

2.6 Immunoblot analysis

Immunoblot analysis was performed as described [17]. We took photographs using LuminoGraph I (ATTO) and performed quantitative analyses of the images using Fiji (https://imagej.net/software/Fiji/). Antibodies and concentrations are summarized in **Table S1**.

2.7 Real-time quantitative PCR

We performed the extraction of total RNA, reverse transcription to cDNA and real-time fluorescence quantitative PCR, as described [24]. The primers used are listed in **Table S2**.

2.8 Mesothelioma tissue array

As previously reported [25], MM formalin-fixed paraffin-embedded (FFPE) samples were prepared as tissue arrays. We selected areas containing MMs based on the observation after hematoxylin and eosin (H&E) staining. Afterwards, cores of 6 mm in diameter were punched out with a tissue microprocessor (KIN-II type, Azumaya Medical Machine). Finally, 12 cores were re-embedded in a new paraffin block. Tissue

sections of 4-μm thickness were then used for H&E staining, Berlin blue staining and immunohistochemistry (IHC) as described [6].

2.9 Immunohistochemistry (IHC) and quantitative analysis

We performed immunostaining procedures using BOND MAX/III (Leica Microsystems) with BOND Polymer Refine Detection (DS9800, Leica) according to the manufacturer's instructions. Photographs of the mounted slides were taken with an Olympus microscope (BX53) and DP22/U-TV0.5XC-3 camera, and quantified using Fiji. We fixed the conditions when taking and processing the photos. Quantification was based on counting positively stained areas in three randomly selected fields and the total cell numbers. Antibodies and concentrations are listed in **Table S1**.

2.10 FerroOrange assay

FerroOrange (RhoNox-4; Goryokayaku) was used to detect cellular catalytic Fe(II) as described [26]. Five random areas were selected and quantified with Fiji.

2.11 Array-based comparative genomic hybridization (aCGH)

We performed aCGH using SurePrint G3 Rat Genome CGH Microarray Kit, 4x180K (G4841A; Agilent Technologies), following the protocols formerly described [17, 24]. A total number of 16 MM samples were analyzed, of which 4 were from MM induced by crocidolite (2 each from *Brca1* Mut and *wild-type* males), and the remaining 12 were from chrysotile-induced mesothelioma (3 each from *Brca1* Mut/*wild-type* and males/females). The control samples were kidneys from 5-week-old rats of the matched genotype/sex. Of these 16 MM samples, 4 (4/16) were EM, 8 (8/16) were SM and 4 (4/16) were BM. Genome copy number aberration and hierarchical clustering analysis were conducted as described [6].

2.12 Fluorescent in situ hybridization (FISH)

We processed 4 μm-thick paraffin-embedded tissue array sections and hybridized them with rat *Cdkn2a* (Cy3)/Chr5CEN (SpectrumGreen) dual color FISH probes (Chromosome Science Labo Inc.; Sapporo, Japan). The detailed procedures have been previously described [17]. The stained specimens were observed and photographed with a BZ-X800 microscope (Keyence). The number of nuclei counted was > 20 per specimen. *Cdkn2a* homozygous deletion was defined as the average ratio of *Cdkn2a*/Chr5CEN ≤ 0.35 whereas hemizygous deletion was defined as the ratio between 0.35 and 0.64. No deletion was assigned when the ratio was ≥ 0.65.

2.13 BAP1 sequence analysis

We selected 14 MM samples (7 each from *Brca1* Mut and *wild-type*). Seven pairs of primers were designed (**Table S2**) and used for PCR amplification of cDNA after RNA extraction and reverse transcription. PCR products encompassing the entire *BAP1* coding exons and 5′ and 3′ untranslated regions were then purified with GenElute™ PCR Clean-Up kit (NA1020, Sigma-Aldrich) and subjected to Sanger sequencing. Sequencing results were standardized by cDNA accession no. NM_001107292.1 as reference.

2.14 Statistical analysis

We performed statistical analysis using an unpaired *t*-test, *Log-rank* (*Mantel-Cox*) test, and *Pearson's chi-square* test using Prism 9.3.1 (Graphpad Prism). Significance of difference (*p* value) was calculated and defined either as **p*<0.05, ***p*<0.01, ****p*<0.001 or no significance (n.s.). Error bar is shown as means ± SEM unless otherwise specified.

3. Results

3.1 Brca1 Mutant rats are more likely to develop MM with higher malignancy

In the carcinogenesis experiment, peritoneal MMs developed in 26/37 (70.2%) and 27/37 (72.9%) rats of *Brca1* Mut and *wild-type* rats in total, respectively **(Figure 1A; Table 1, S3)**. In contrast, no MM occurred in the control group at the end of the experiment (maximum of 110 weeks after birth). Although there was no significant difference in the overall MM incidence, the mortality by MMs was significantly earlier in the *Brca1* Mut group, especially in male rats injected with chrysotile **(Figure 1AB)**. No significant differences were observed in the remaining groups **(Figure S1CD)**. Changes in body weight also reflected this survival rate difference. Except for *Brca1* Mut/male/chrysotile group, which showed a significant increase in body weight by ascites compared to the *wild-type* groups **(Figure S1E)**, there was no difference in the body weight among other groups.

We observed only MMs as neoplasm in the whole experiments. Histologically, we confirmed the morphology **(Figure 1C, S2A)** and the mesothelial markers (mesothelin, podoplanin, cytokeratin AE1/AE3, calretinin, and vimentin) in MM samples **(Figure S2B)**. Nuclear atypia, along with the frequency of mitosis, was summed up as the nuclear grade of each tumor **(Figure S2CD)**. Consistent with the MM mortality, nuclear grade was significantly higher in the *Brca1* Mut/male/chrysotile group than the *wild-type* **(Figure S2D)**. Also, chrysotile-induced MMs showed a tendency of higher nuclear grade compared to crocidolite **(Figure S2D)**. The nuclear grade was significantly correlated with the lifespan of rats **(Figure S2E)**.

Compared to the *wild-type*, the *Brca1* Mut group revealed similar fractions of EM and no-malignancy but a higher fraction of SM as well as a lower proportion of BM **(Figure 1D)**, indicating promotion of epithelial-mesenchymal transition (EMT) in *Brca1*

Mut rats. Higher expression of vimentin, a mesenchymal marker, confirmed stronger EMT in *Brca1* Mut MMs **(Figure S2F)**. MMs in both Mut and *wild-type* presented increased Brca1 expression in comparison to non-tumorous mesothelium **(Figure 1E)**, indicating that the normal *Brca1* allele is not lost, confirming haploinsufficiency. Higher nuclear Ki-67 positivity **(Figure 1F)** was characteristic of *Brca1* Mut MMs, regardless of the type of asbestos injected, implying a more active proliferation of tumors.

3.2 BRCA1 haploinsufficiency promotes chromosomal deletion, especially Cdkn2a/2b

Brca1 haploinsufficiency impairs genome stability through insufficient DNA damage repair, leading to an increased possibility of genome alterations [27]. As results of aCGH (GEO accession: GSE210598), *Brca1* Mut MMs showed more amplifications on chromosomes 1, 4, 12, and 15 and deletions on chromosomes 5, 7, 8, and 14 **(Figure 1G, S3A)**. Meanwhile, *Brca1* Mut MMs presented a marginally significant increase in the genomic length of chromosomal deletion ($p = 0.1407$) **(Figure S3B)**. SM MMs showed more genome DNA amplifications/deletions in comparison to EM **(Figure S3A)**.

Cdkn2a/2b was more likely to be deleted in *Brca1* Mut MMs than *wild-type*. At chromosome region 5q32, both *Brca1* Mut and *wild-type* MMs exhibited deletions of *Cdkn2a/2b* **(Figure 1G)**, the best-known signature of genomic variations in human mesothelioma at chromosome region 9p21 [28, 29]. Deletion of *Cdkn2a/2b* existed in all *Brca1* Mut MMs (8/8) compared to 50% (4/8) in *wild-type* ($p = 0.0082$), which partially explained the earlier onset of MMs in *Brca1* Mut rats. FISH analysis on the *Cdkn2a* locus further confirmed more *Cdkn2a* deletions in *Brca1* Mut MMs [9/12 (75%)] than *wild-type* [5/13 (38.5%)] ($p = 0.1107$) **(Figure 1H; Table S4)**. In terms of asbestos types, *Cdkn2a* deletion ratio of chrysotile-induced MMs significantly differed between *Brca1* Mut and *wild-type* ($p = 0.0012$) compared to crocidolite groups ($p = 0.9157$) **(Table S5)**. We also

screened for additional oncogenes and tumor suppressor genes, which revealed significant variations **(Figure S3C)**.

3.3 Alteration of BRCA1 expression under BRCA1 haploinsufficiency in mesothelium during MMs carcinogenesis in response to different fibers

To study BRCA1 under BRCA1 haploinsufficiency, we quantified total BRCA1 expression at various time-points during mesothelial carcinogenesis. In *Brca1* Mut MMs, total BRCA1 expression showed no significant difference from that in *wild-type* MMs **(Figure 2A)**, consistent with immunoblot results **(Figure 1E)**. However, BRCA1 expression revealed a proportional correlation with the rat survival **(Figure 2B)** and an inverse correlation with MM nuclear grade **(Figure 2C)**. Unlike BRCA1, pBRCA1 expression was significantly reduced in *Brca1* Mut MMs **(Figure 2D)**. Chrysotile-induced *Brca1* Mut MMs showed both lower BRCA1 and pBRCA1 expression than those by crocidolite **(Figure 2A, 2D)**. Also, γ-H2AX, a marker of DNA DSBs [30], was significantly increased in *Brca1* Mut MMs of both asbestos **(Figure 2E)**.

We next searched for the BRCA1 expression alterations under BRCA1 haploinsufficiency in the early phase after asbestos exposure. During subacute experiment, BRCA1 expression in *Brca1* Mut mesothelium was persistently lower than that of *wild-type*, which was progressively emphasized over time **(Figure 3A)**. Tendency of pBRCA1 expression was similar to that of total BRCA1 **(Figure 3B)**. Particularly, mesothelium 2 y after chrysotile exposure showed significantly lower BRCA1 expression in comparison to crocidolite **(Figure 3A)**. After acute exposure of chrysotile to cultured mesothelial cells, BRCA1/pBRCA1 expression were persistently lower in *Brca1* Mut primary cultured mesothelial cells than *wild-type* cells **(Figure 3C)**.

3.4 BRCA1 haploinsufficiency impairs iron metabolism during MM

development

Hierarchical clustering of the aCGH results on iron metabolism-related genes recognized differences between *Brca1* Mut and *wild-type* in general **(Figure S4A).** Particularly remarkable were the changes in *Tfr2*, which exhibited more amplification in chrysotile-induced *Brca1* Mut MMs (3/6) than that of wild-type (1/6) **(Figure 1G, S4A).**

In *Brca1* Mut MMs, expression of both *Tfr1* and *Tfr2* mRNA **(Figure S4B)** and protein **(Figure 4A, 4B)** were higher than those of *wild-type* MMs. Higher expression of transferrin receptors was positively associated with an increase in intracellular Fe(II), which was verified in the MM cell lines detected by FerroOrange **(Figure 4C)**. Excessive intracellular Fe(II) deactivated the IRE/IRP system as a feedback, as demonstrated by the reduced expression of IRP1 **(Figure S4C)**, which was consistent with the higher *Tfr1* mRNA level of *Brca1* Mut MM in comparison to the *wild-type* **(Figure S4B)**. Insoluble intracellular Fe(Ⅲ) as seen by Berlin blue revealed reduced iron store in *Brca1* Mut MMs **(Figure 4D)**. Decreased level of FTL and FTH expression by IHC staining and immunoblot analysis confirmed lowered Fe(III) reserve in *Brca1* Mut MMs **(Figure 4E, S4C)**.

In the subacute phase, BRCA1 haploinsufficiency also altered iron metabolism. After *ip* injection of crocidolite or chrysotile, Tfr1 expression significantly increased in *Brca1* Mut mesothelium in comparison to *wild-type* **(Figure 5A)**. However, Tfr2 revealed no significant changes in the subacute phase **(Figure 5B)**. Similar changes also existed in the immunoblot analysis of mesothelium **(Figure S4D)**. Chrysotile injection showed higher expression of Tfr1 compared to crocidolite **(Figure 5A)**, reflecting the higher iron released by hemolysis [31, 32]. There is little insoluble Fe(III) accumulation in the subacute period whereas significant amounts of Fe(III) were deposited in the mesothelium at the chronic period of ~2 y **(Figure 5C)**, demonstrating that iron deposition is a chronic process. Also, consistent with the MM findings, BRCA1 haploinsufficiency caused a shortage of stored Fe(III) storage in non-tumorous mesothelial cells compared with *wild-*

type **(Figure 5C, S4E)**.

3.5 BRCA1 haploinsufficiency induces ferroptosis-resistance after asbestos exposure

Finally, we evaluated the involvement of ferroptosis in BRCA1 haploinsufficiency-related mesothelioma development. Higher amounts of 8-OHdG, an oxidative stress marker [33], was found only in chrysotile-induced *Brca1* Mut MMs **(Figure 6A)**, indicating that *Brca1* Mut mesothelial cells exposed to chrysotile transformed into MMs with higher oxidative stress. The MMs revealed only silent somatic mutations in *BAP1* **(**3/7 in Mut, 1/7 in *wild-type*; **Figure S5A)** with alternatively spliced mRNA (XM_006252607.3; skipped codon 23-35). Regarding ferroptosis, we found that BAP1 expression significantly decreased in *Brca1* Mut MMs, accompanied by elevated expression of xCT and GPX4 **(Figure 6B, S5BCD)**. Thus, MM cells established ferroptosis-resistance and exhibited lower levels of ferroptosis markers, such as HNEJ-1 and PTGS2 [34, 35] **(Figure 6C, 6D)**.

We likewise compared the subacute response of mesothelial cells to chrysotile/crocidolite in *Brca1* Mut and *wild-type* rats. BRCA1 haploinsufficiency led to reduced expression of BAP1 **(Figure S5E)**. In the oxidative environment caused by asbestos **(Figure 7A)**, *Brca1* Mut mesothelial cells exhibited higher levels of GPX4 and xCT compared to the *wild-type* **(Figure 7BC)**. Of note, chrysotile-exposed mesothelial cells exhibited higher expression of xCT in both subacute and chronic phases **(Figure 7B)** as well as GPX4 **(Figure 7C)** in the chronic phase in comparison to crocidolite. *Brca1* Mut primary mesothelial cells also manifested a decrease in PTGS2 and ACSL4 expression whereas those in *wild-type* increased after applying chrysotile **(Figure 7D)**.

4. Discussion

We for the first time found that *Brca1* male mutant is a risk for chrysotile-induced mesothelial carcinogenesis, using a recently established rat model which reproduces human phenotype [15, 17]. The incidence of MM was significantly promoted with shorter survival though the final incidence was not significantly altered between the Mut and *wild-type*, indicating that a combination of chrysotile and *Brca1* Mut male has a promotional but not an initiation effect. Similar tendency was observed also for crocidolite and/or females. This male preponderance is the same for humans [22], which needs further investigation from the viewpoint of sex hormones.

Interestingly, Brca1 expression was maintained in all the MMs examined in the present experiment. Therefore, *Brca1* tumor suppressor gene works as haploinsufficiency, not as complete loss, whereas expression of Brca1 and pBrca1 was significantly lower for the MMs of chrysotile and/or Mut. This suggests that residual Brca1 is beneficial for MM growth. Furthermore, incidence of homozygous deletion of *Cdkn2a/2b* was significantly higher for the MMs of Brca1 Mut than those of *wild-type*, confirming the importance of DNA DSB repair. Indeed, fraction of γ-H2AX-or 8-OHdG-positive MM cells was significantly higher in the Mut, suggesting that Mut causes more mutagenic environment under asbestos exposure. With aCGH analysis, total genomic length of deleted areas was marginally increased in the MMs of *Brca1* Mut, presumably because shorter genome is advantageous for faster cellular proliferation by completing genome replication earlier. Cell proliferation of MM in the Mut as evaluated by Ki67 was significantly higher for the Mut with higher incidence of EMT, representing more aggressive behavior of the tumor. We could confirm corresponding results on Brca1 expression in the mesothelial cells of subacute phase as well.

Next, we analyzed the MM carcinogenesis from the standpoint of iron metabolism. As we reported, derangement of iron metabolism is the key pathogenic mechanism for asbestos-induced carcinogenesis both on mesothelial cells [6, 8] and macrophages [36-38]. Iron

addiction with ferroptosis-resistance may represent the pathogenesis [39, 40]. All the asbestos fibers have high affinity for hemoglobin and histones [32, 41], and mesothelial cells are also phagocytic cells [5, 42], which constitute the essential portion of carcinogenesis via physical breakage of the genome by iron-coated scissor-like asbestos fibers [7]. Recently, we found that macrophages fall into ferroptosis during the scavenging process of iron-coated asbestos fibers [36], which still emits exosomes filled with Fe(III)-loaded ferritin to the target mesothelial cells, causing oxidative stress [37, 43]. The difference in iron metabolism was distinct between the *Brca1* Mut MMs and those from *wild-type*. Mut MMs held higher catalytic Fe(II) with high Tfr1/Tfr2 levels but showed lower insoluble Fe(III) and ferritin levels. This was not different between chrysotile and crocidolite and indicates that the turnover and metabolically available iron is significantly higher in Mut MMs than those of *wild-type*. Notably, some of the Mut MMs showed genomic amplification of Tfr2, especially for chrysotile-induced MMs, which we believe works for the regulation of excess iron [44]. Difference in the expression of Tfr1 between Mut and *wild-type* was observed at the subacute phase, but Fe(III) deposition in the mesothelium was found exclusively at 2 y, suggesting that ultimate alteration of iron metabolism takes a long time.

Finally, we evaluated the difference in ferroptosis-resistance [8] depending on fibers during MM carcinogenesis. Ferroptosis is a recently established concept of cell death defined by catalytic Fe(II)-dependent regulated necrosis accompanied by lipid peroxidation [35, 40, 45]. Whereas chrysotile-induced Mut MMs were more oxidatively stressed as seen by 8-OHdG [46] than the other groups, they simultaneously revealed more ferroptosis-resistance by a variety of factors we examined, including decreased BAP1 [47] and increased xCT (Slc7A11) [48] and GPX4 [49]. We recently developed a monoclonal antibody, HNEJ-1 [50, 51], to detect ferroptosis [34], which also demonstrated ferroptosis-resistance in MMs especially of chrysotile/Mut along with PTGS2 [52, 53]. The same tendency to be more ferroptosis-resistant for chrysotile/Mut was observed also in the

subacute experiments and cultured mesothelial cell experiments, which suggests that BRCA1 haploinsufficiency predisposes to BAP1 deficiency though further study is necessary. We believe that this is associated with the physical characteristics of chrysotile [22], which is more elastic than crocidolite and can cause hemolysis [31] **(Figure 8)**. Mitochondria, major organellae for heme synthesis and iron metabolism, may be critical for establishing ferroptosis-resistance as in the case of ferric nitrilotriacetate-induced renal carcinogenesis [17].

In summary, Brca1 haploinsufficiency in rats promoted chrysotile-induced mesothelial carcinogenesis in males **(Figure 8)**. Therefore, chrysotile exposure can be a higher but avoidable risk for MM in *BRCA1* mutant males than the general population. Although there is thus far no report on MM in germline *BRCA1* mutants, it may be just overlooked due to the rarity of this cancer. The limitations of the present study are that this is a preclinical study using rat models and that the route of asbestos administration is intraperitoneal, which is an efficient method to expose asbestos directly to mesothelial cells.

Disclosure

Funding Information: This work was supported in part by JST CREST (JPMJCR19H4), JSPS Kakenhi (JP19H05462 and JP20H05502) to ST, JSPS Kakenhi (JP16H06276 [AdAMS]) to TM and JP21H03601 to TI, and JST SPRING (JPMJSP2125) to YL.

Conflict of Interest: ST is the associate editor of Cancer Science. The remaining authors have no conflict of interest.

Ethics Statement: Approval of the research protocol by an Institutional Reviewer Board, N/A; Informed Consent, N/A; Registry and Registration of the No. of the study/trial, N/A; Animal Studies, this study was approved by the animal experiment committee of Nagoya University Graduate School of Medicine.

Author contribution: YL and ST, conception and design of the study; YL, SA, YM, YK,

HZ and ST, acquisition and analysis of the data; YL, SA and ST, drafting the manuscript and the figures; TM and TI: supply of the *Brca1 (L63X/+)* mutant rat.

Acknowledgments

The author (YL) would like to thank the "Interdisciplinary Frontier Next-Generation Researcher Program of the Tokai Higher Education and Research System. The authors thank Nobuaki Misawa (Department of Pathology and Biological Responses, Nagoya University Graduate School of Medicine) for excellent technical assistance, and also Division for Medical Research Engineering, Nagoya University Graduate School of Medicine for technical assistance.

Figure legends

Figure 1 BRCA1 haploinsufficiency promotes chrysotile-induced malignant mesothelioma (MM) in males. (A) Probability of MM development in *Brca1(L63X/+)* (Mut; N = 7) and *wild-type* (WT; N = 8) male rats injected with chrysotile (*Brca1* Mut *vs.* *wild-type*; $p = 0.0289$, χ^2 test). Untreated *Brca1* Mut (N = 10) and *wild-type* (N = 10) rats are shown as dotted lines. (B) *Kaplan-Meier* curves show the survival rate of *Brca1* Mut (N = 7) and *wild-type* (N = 8) male rats injected with chrysotile (*Brca1* Mut *vs.* wild-type; $p = 0.0358$, Log-rank test). (C) Representative case of MMs in macroscopic image (bar = 1 cm), H&E staining of epithelioid (EM) and sarcomatoid (SM) subtypes (bar = 50 μm). (D) Proportions of various subtypes (BM, biphasic) in MM of *Brca1* Mut and *wild-type*, irrespective of asbestos and sex. (E) Immunoblot analysis of BRCA1 expression of mesothelium and MM samples. (F) IHC analysis of Ki-67 on MM samples (bar = 25μm; N ≧ 7). (G) Array-based CGH analysis of MMs induced from *Brca1* Mut or *wild-type* male rats by chrysotile (N = 3). Gains or losses are expressed as the logarithm of base 2. Callouts show *Cdkn2a/2b* deletion and *Tfr2* amplification, respectively. (H) Representative images of fluorescent *in situ* hybridization to confirm homozygous deletion of *Cdkn2a.* Red (*Cdkn2a*) and green (chromosome 5 centromere) dots are counterstained by blue (nucleus). Normal diploids (left panel), heterozygous deletion (center panel) and homozygous deletion (right panel) are shown. CGH, comparative genomic hybridization; Cro, crocidolite; Chry, chrysotile.

Figure 2 Chrysotile-induced MMs present lower expression of Brca1. (A) IHC staining of total BRCA1 on MM samples (bar = 25 μm; N ≧ 7). (B) Correlation between expression of total BRCA1 and survival probability (N = 34; $p = 0.0267$, *Pearson*'s rank correlation coefficient = 0.3799). (C) Correlation between BRCA1 expression and nuclear grade (N = 34; $p = 0.0017$, *Pearson*'s rank correlation coefficient = -0.5169). (D,

E) IHC staining of phospho-BRCA1 (Ser1423) and phospho-H2AX (Ser139) on MM samples (N ≧ 7). IHC, immunohistochemistry.

Figure 3 BRCA1 expression is reduced in *Brca1* Mut mesothelium in the subacute phase after asbestos exposure. (A, B) IHC staining with total BRCA1 and phospho-BRCA1 (Ser1423) for mesothelium at subacute (4 weeks) and chronic (2 y) phases (bar = 25 μm; N ≧ 3). The callout shows mesothelial layers that were numerically processed, same as below. (C) Changes in BRCA1 and p-BRCA1 expression over time after applying chrysotile to primary cultured mesothelial cells (N = 3). Note that the same immunoblot membrane was used as in Figure 7D and S4E.

Figure 4 BRCA1 haploinsufficiency alters iron metabolism to cause an increase in Fe(II) and a decrease in Fe(III) in asbestos-induced MMs. (A, B) IHC staining of transferrin receptor 1 (Tfr1) and transferrin receptor 2 (Tfr2) on MM samples (bar = 25 μm; N ≧ 7). (C) Mesothelin IHC and RhoNox-4 (FerroOrange) fluorescent staining of chrysotile-induced mesothelioma cell lines (N = 4). (D) Berlin blue staining on MM samples (N ≧ 7). (E) IHC staining of ferritin light chain on MM samples (N ≧ 7).

Figure 5 BRCA1 haploinsufficiency promotes iron uptake in the subacute phase of asbestos-induced mesothelial carcinogenesis. (A, B) IHC staining with Tfr1 and Tfr2 for mesothelium at subacute (4 weeks) phase (bar = 25 μm; N ≧ 3). (C) Berlin blue staining for mesothelium at subacute (4 weeks) and chronic (2 y) phases (N ≧ 3).

Figure 6 High oxidative stress with ferroptosis-resistance in asbestos-induced *Brca1* Mut MMs. (A) IHC of 8-OHdG on MM samples (N ≧ 7). (B) Immunoblot analysis of ferroptosis-related proteins (BAP1, xCT, and GPX4) expression in mesothelium and MM samples (bar = 25 μm). (C, D) IHC of HNEJ-1 and PTGS2 on MM samples (N ≧

7). 8-OHdG, 8-hydroxy-2'-deoxyguanosine; BAP1, BRCA1-associated protein 1; xCT, cystine/glutamate transporter; GPX4, glutathione peroxidase 4; PTGS2, prostaglandin-endoperoxide synthase 2.

Figure 7 High oxidative stress with ferroptosis-resistance in the subacute phase of asbestos-induced mesothelial carcinogenesis. (A) IHC of 8-OHdG for mesothelium at subacute (4 weeks) phase (bar = 25 μm; N ≧ 3). (B, C) IHC staining with xCT and GPX4 for mesothelium at subacute (4 weeks) and chronic (2 y) phases (N ≧ 3). (D) Time-course immunoblot of ACSL4 and PTGS2 expression in primary cultured mesothelial cells exposed to chrysotile (N = 3). ACSL4, acyl-CoA synthetase long-chain family member 4. Note that the same immunoblot membrane was used as in Figure 3C and S4E.

Figure 8 Overview schema of how BRCA1 haploinsufficiency influences development of MMs.

List of supporting information

Table S1 Antibodies used for immunoblotting and IHC staining

Table S2 Nucleotide sequences of primers

Table S3 Details of MMs induced by crocidolite or chrysotile in this article (Refer to Fig. S2 for details)

Table S4 Summary of FISH analysis on *Cdkn2a* deletion in crocidolite or chrysotile-induced MMs

Table S5 Incidence of *Cdkn2a* deletion (homozygous/hemizygous deletion) in terms of asbestos types in total (sum of aCGH and FISH)

Table S6 Summary of MM metastasis and other tumors obtained in the carcinogenesis experiment.

Figure S1 Supplementary figures for carcinogenesis experiment.

Figure S2 Supplementary images for mesothelioma morphology.

Figure S3 Quantitative analysis of array-based CGH (aCGH) analysis and hierarchical clustering analysis.

Figure S4 Supplementary data on iron metabolism changes.

Figure S5 Supplementary data on investigation for ferroptosis resistance.

References

1. IARC WHO. Asbestos (chrysotile, amosite, crocidolite, tremolite, actinolite, and anthophyllite). IARC Monographs on the Evaluation of Carcinogenic Risks to Humans A Review of Human Carcinogens; Part C: Arsenic, Metals, Fibres, and Dusts. Lyon, France, 2012; 219-309.
2. Thives LP, Ghisi E, Thives Junior JJ, Vieira AS. Is asbestos still a problem in the world? A current review. J Environ Manage. 2022; 319: 115716.
3. Jiang Z, Chen J, Chen J, et al. Mortality due to respiratory system disease and lung cancer among female workers exposed to chrysotile in Eastern China: A cross-sectional study. Front Oncol. 2022; 12: 928839.
4. Hodgson JT, McElvenny DM, Darnton AJ, Price MJ, Peto J. The expected burden of mesothelioma mortality in Great Britain from 2002 to 2050. Br J Cancer. 2005; 92: 587-93.
5. Jiang L, Nagai H, Ohara H, et al. Characteristics and modifying factors of asbestos-induced oxidative DNA damage. Cancer Sci. 2008; 99: 2142-51.
6. Jiang L, Akatsuka S, Nagai H, et al. Iron overload signature in chrysotile-induced malignant mesothelioma. J Pathol. 2012; 228: 366-77.
7. Toyokuni S. Mechanisms of asbestos-induced carcinogenesis. Nagoya J Med Sci. 2009; 71: 1-10.
8. Toyokuni S. Iron addiction with ferroptosis-resistance in asbestos-induced mesothelial carcinogenesis: Toward the era of mesothelioma prevention. Free Radic Biol Med. 2019; 133: 206-15.
9. Yoshida R. Hereditary breast and ovarian cancer (HBOC): review of its molecular characteristics, screening, treatment, and prognosis. Breast Cancer. 2021; 28: 1167-80.
10. Deng CX. BRCA1: cell cycle checkpoint, genetic instability, DNA damage response and cancer evolution. Nucleic Acids Res. 2006; 34: 1416-26.
11. Betti M, Casalone E, Ferrante D, et al. Germline mutations in DNA repair genes predispose asbestos-exposed patients to malignant pleural mesothelioma. Cancer Lett. 2017; 405: 38-45.
12. Jensen DE, Proctor M, Marquis ST, et al. BAP1: a novel ubiquitin hydrolase which binds to the

BRCA1 RING finger and enhances BRCA1-mediated cell growth suppression. Oncogene. 1998; 16: 1097-112.

13. Testa JR, Cheung M, Pei J, et al. Germline BAP1 mutations predispose to malignant mesothelioma. Nat Genet. 2011; 43: 1022-5.

14. Evers B, Jonkers J. Mouse models of BRCA1 and BRCA2 deficiency: past lessons, current understanding and future prospects. Oncogene. 2006; 25: 5885-97.

15. Nakamura Y, Kubota J, Nishimura Y, et al. Brca1(L63X) (/+) rat is a novel model of human BRCA1 deficiency displaying susceptibility to radiation-induced mammary cancer. Cancer Sci. 2022; 113: 3362-75.

16. Toyokuni S, Kong Y, Cheng Z, et al. Carcinogenesis as Side Effects of Iron and Oxygen Utilization: From the Unveiled Truth toward Ultimate Bioengineering. Cancers (Basel). 2020; 12: 3320.

17. Kong Y, Akatsuka S, Motooka Y, et al. BRCA1 haploinsufficiency promotes chromosomal amplification under Fenton reaction-based carcinogenesis through ferroptosis-resistance. Redox Biol. 2022; 54: 102356.

18. Toyokuni S, Kong Y, Zheng H, Maeda Y, Motooka Y, Akatsuka S. Iron as spirit of life to share under monopoly. J Clin Biochem Nutr. 2022; 71: 78-88.

19. Nagai H, Okazaki Y, Chew SH, Misawa N, Yasui H, Toyokuni S. Deferasirox induces mesenchymal-epithelial transition in crocidolite-induced mesothelial carcinogenesis in rats. Cancer Prev Res. 2013; 6: 1222-30.

20. Ohara Y, Chew SH, Shibata T, Okazaki Y, Yamashita K, Toyokuni S. Phlebotomy as a preventive measure for crocidolite-induced mesothelioma in male rats. Cancer Sci. 2018; 109: 330-9.

21. Jiang L, Yamashita Y, Toyokuni S. A novel method for efficient collection of normal mesothelial cells in vivo. J Clin Biochem Nutr. 2010; 46: 265-8.

22. Oury TD, Sporn TA, Roggli VL (Eds). Pathology of Asbestos-Associated Diseases, Third edition. Berlin/Heidelberg: Springer, 2014.

23. Kajiyama H, Kikkawa F, Maeda O, Suzuki T, Ino K, Mizutani S. Increased expression of

dipeptidyl peptidase IV in human mesothelial cells by malignant ascites from ovarian carcinoma patients. Oncology-Basel. 2002; 63: 158-65.

24. Cheng Z, Akatsuka S, Li GH, Mori K, Takahashi T, Toyokuni S. Ferroptosis resistance determines high susceptibility of murine A/J strain to iron-induced renal carcinogenesis. Cancer Sci. 2022; 113: 65-78.

25. Nagai H, Okazaki Y, Chew S, et al. Diameter of multi-walled carbon nanotubes is a critical factor in mesothelial injury and subsequent carcinogenesis. Proc Natl Acad Sci U S A. 2011; 108: E1330-8.

26. Yue L, Luo Y, Jiang L, Sekido Y, Toyokuni S. PCBP2 knockdown promotes ferroptosis in malignant mesothelioma. Pathol Int. 2022; 72: 242-51.

27. Yoshida K, Miki Y. Role of BRCA1 and BRCA2 as regulators of DNA repair, transcription, and cell cycle in response to DNA damage. Cancer Sci. 2004; 95: 866-71.

28. Illei PB, Rusch VW, Zakowski MF, Ladanyi M. Homozygous deletion of CDKN2A and codeletion of the methylthioadenosine phosphorylase gene in the majority of pleural mesotheliomas. Clin Cancer Res. 2003; 9: 2108-13.

29. Lopez-Rios F, Chuai S, Flores R, et al. Global gene expression profiling of pleural mesotheliomas: overexpression of aurora kinases and P16/CDKN2A deletion as prognostic factors and critical evaluation of microarray-based prognostic prediction. Cancer Res. 2006; 66: 2970-9.

30. Kuo LJ, Yang LX. Gamma-H2AX - a novel biomarker for DNA double-strand breaks. In Vivo. 2008; 22: 305-9.

31. Harington JS, Miller K, Macnab G. Hemolysis by asbestos. Environ Res. 1971; 4: 95-117.

32. Nagai H, Ishihara T, Lee WH, et al. Asbestos surface provides a niche for oxidative modification. Cancer Sci. 2011; 102: 2118-25.

33. Toyokuni S, Tanaka T, Hattori Y, et al. Quantitative immunohistochemical determination of 8-hydroxy-2'-deoxyguanosine by a monoclonal antibody N45.1: its application to ferric nitrilotriacetate-induced renal carcinogenesis model. Lab Invest. 1997; 76: 365-74.

34. Zheng H, Jiang L, Tsuduki T, Conrad M, Toyokuni S. Embryonal erythropoiesis and aging

exploit ferroptosis. Redox Biol. 2021; 48: 102175.

35. Stockwell BR. Ferroptosis turns 10: Emerging mechanisms, physiological functions, and therapeutic applications. Cell. 2022; 185: 2401-21.

36. Ito F, Yanatori I, Maeda Y, et al. Asbestos conceives Fe(II)-dependent mutagenic stromal milieu through ceaseless macrophage ferroptosis and beta-catenin induction in mesothelium. Redox Biol. 2020; 36: 101616.

37. Ito F, Kato K, Yanatori I, Murohara T, Toyokuni S. Ferroptosis-dependent extracellular vesicles from macrophage contribute to asbestos-induced mesothelial carcinogenesis through loading ferritin. Redox Biol. 2021; 47: 102174.

38. Toyokuni S, Ito F, Motooka Y. Role of ferroptosis in nanofiber-induced carcinogenesis. Metallomics Res. 2021; 1: 14-21.

39. Toyokuni S, Yanatori I, Kong Y, Zheng H, Motooka Y, Jiang L. Ferroptosis at the crossroads of infection, aging and cancer. Cancer Sci. 2020; 111: 2665-71.

40. Toyokuni S, Kong Y, Zheng H, Maeda Y, Katabuchi M, Motooka Y. Three-dimensional regulation of ferroptosis at the intersection of iron, sulfur and oxygen executing scrap and build toward evolution. Antioxid Redox Signal. 2022. doi: 10.1089/ars.2022.0142.

41. Nagai H, Toyokuni S. Differences and similarities between carbon nanotubes and asbestos fibers during mesothelial carcinogenesis: shedding light on fiber entry mechanism. Cancer Sci. 2012; 103: 1378-90.

42. Nagai H, Chew S, Okazaki Y, et al. Metamorphosis of mesothelial cells wtih active horizontal motility in tissue culture. Sci Rep. 2013; 3: 1144.

43. Toyokuni S, Kong Y, Zheng H, et al. Double-edged Sword Role of Iron-loaded Ferritin in Extracellular Vesicles. J Cancer Prev. 2021; 26: 244-9.

44. Kawabata H. Transferrin and transferrin receptors update. Free Radic Biol Med. 2019; 133: 46-54.

45. Stockwell BR, Friedmann Angeli JP, Bayir H, et al. Ferroptosis: A Regulated Cell Death Nexus Linking Metabolism, Redox Biology, and Disease. Cell. 2017; 171: 273-85.

46. Toyokuni S, Okamoto K, Yodoi J, Hiai H. Persistent oxidative stress in cancer. FEBS Lett. 1995;

358: 1-3.

47. Zhang Y, Shi J, Liu X, et al. BAP1 links metabolic regulation of ferroptosis to tumour suppression. Nat Cell Biol. 2018; 20: 1181-92.

48. Dixon SJ, Lemberg KM, Lamprecht MR, et al. Ferroptosis: an iron-dependent form of nonapoptotic cell death. Cell. 2012; 149: 1060-72.

49. Friedmann Angeli JP, Schneider M, Proneth B, et al. Inactivation of the ferroptosis regulator Gpx4 triggers acute renal failure in mice. Nat Cell Biol. 2014; 16: 1180-91.

50. Toyokuni S, Miyake N, Hiai H, et al. The monoclonal antibody specific for the 4-hydroxy-2-nonenal histidine adduct. FEBS Lett. 1995; 359: 189-91.

51. Ozeki M, Miyagawa-Hayashino A, Akatsuka S, et al. Susceptibility of actin to modification by 4-hydroxy-2-nonenal. J Chromatogr B Analyt Technol Biomed Life Sci. 2005; 827: 119-26.

52. Yang WS, SriRamaratnam R, Welsch ME, et al. Regulation of ferroptotic cancer cell death by GPX4. Cell. 2014; 156: 317-31.

53. Jiang L, Kon N, Li T, et al. Ferroptosis as a p53-mediated activity during tumour suppression. Nature. 2015; 520: 57-62.

Table 1 Summary of malignant mesotheliomas (MMs) in asbestos-injected rats

	Brca1 Mut		*Wild-type*	
	Male	Female	Male	Female
Crocidolite	6/10(60.0%)	4/9(44.4%)	6/8(75.0%)	6/8(75.0%)
Chrysotile	7/9(77.8%)	9/9(100.0%)	8/10(80.0%)	7/11(63.6%)
Control	0/10	0/10	0/10	0/10

Brca1 Mut, *Brca1* mutant (L63X/+). Refer to text for details.

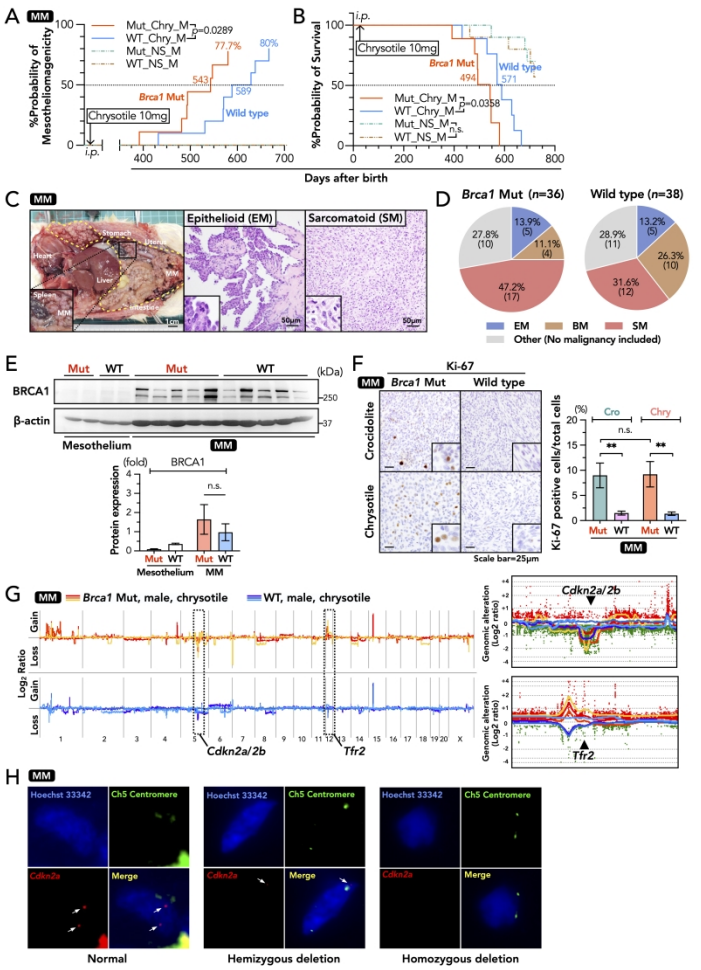

Figure 1

Figure 1

1749x2474mm (72 x 72 DPI)

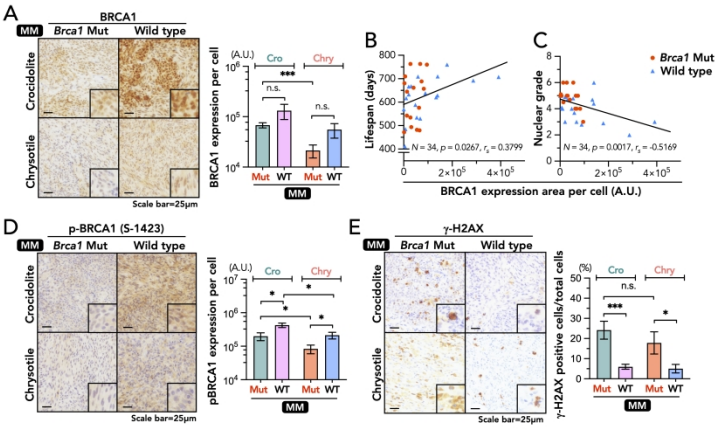

Figure 2

Figure 2

1749x2474mm (72 x 72 DPI)

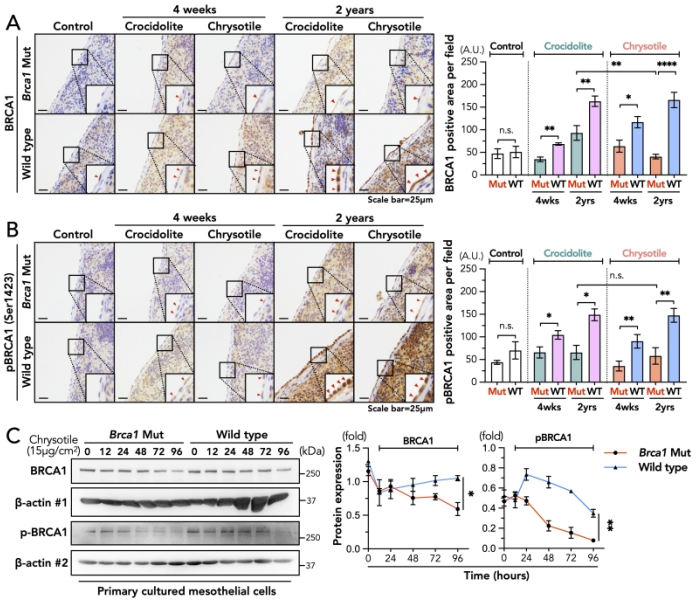

Figure 3

Figure 3

1749x2474mm (72 x 72 DPI)

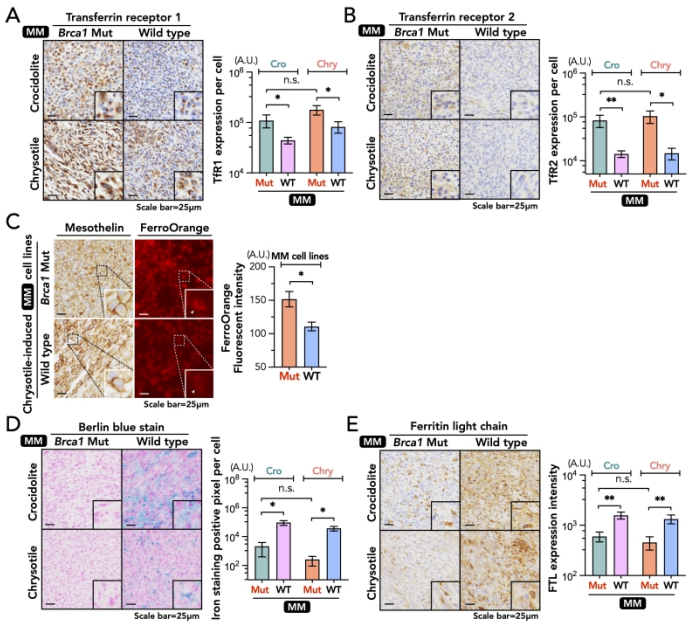

Figure 4

Figure 4

1749x2474mm (72 x 72 DPI)

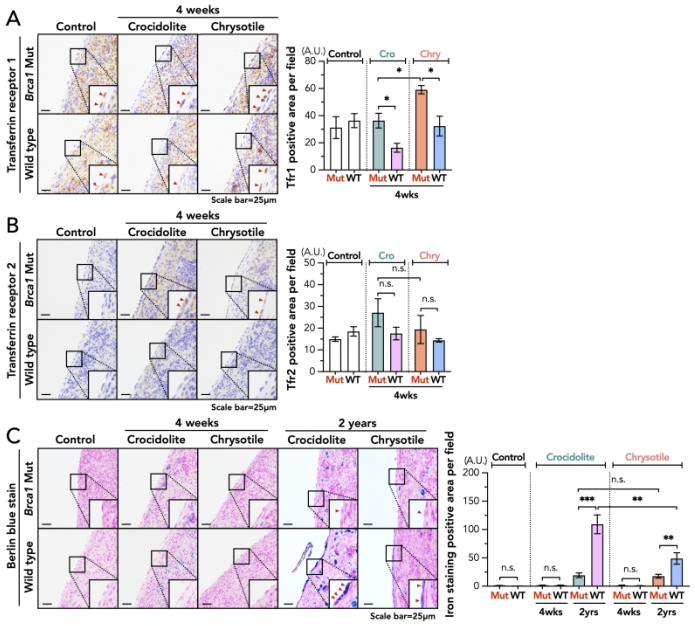

Figure 5

Figure 5

1749x2474mm (72 x 72 DPI)

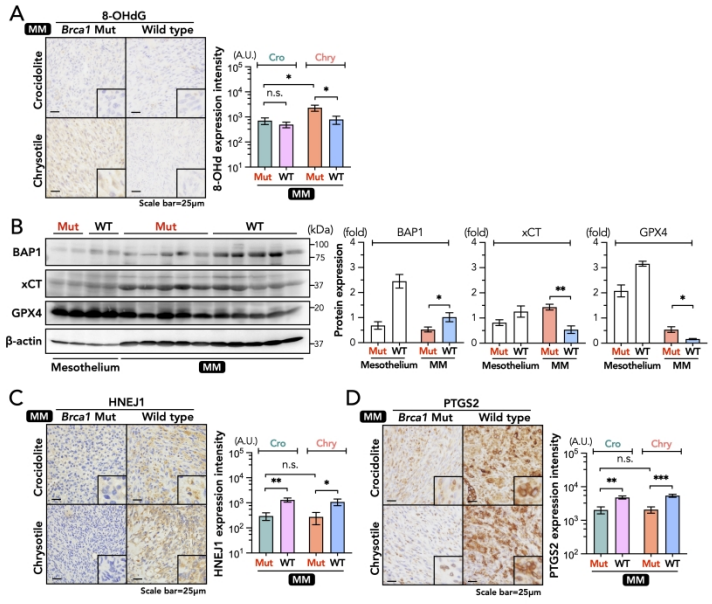

Figure 6

Figure 6

1749x2474mm (72 x 72 DPI)

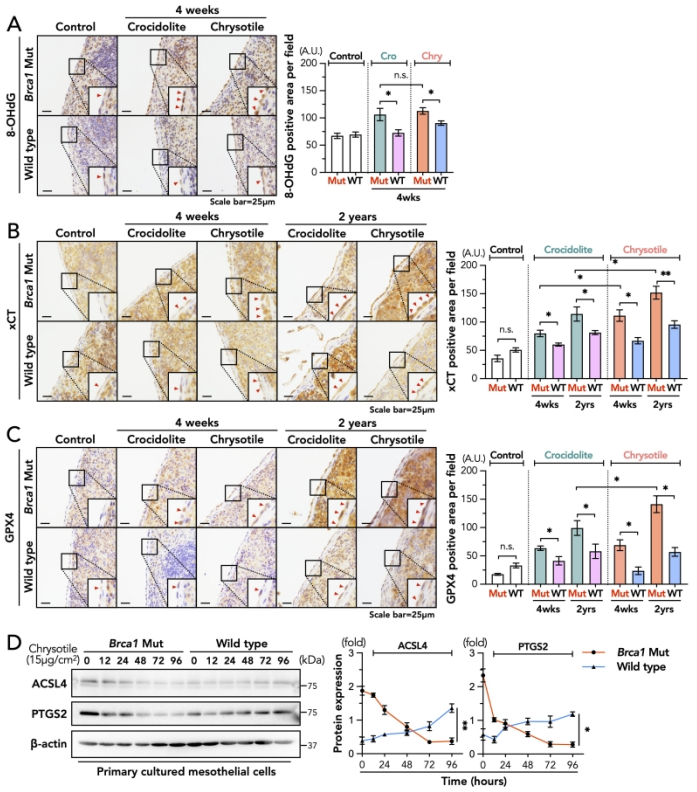

Figure 7

Figure 7

1749x2474mm (72 x 72 DPI)

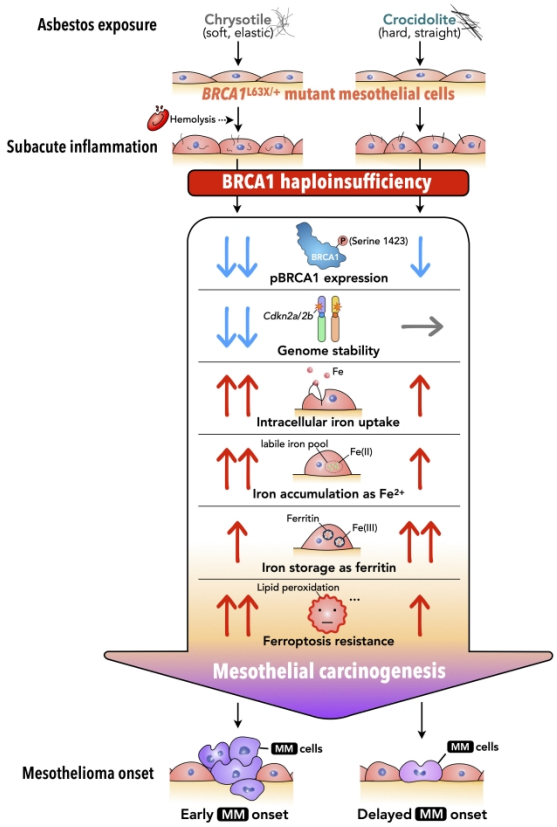

Figure 8

Figure 8

1749x2474mm (72 x 72 DPI)